

Article

Mapping Local Climate Zones Using ArcGIS-Based Method and Exploring Land Surface Temperature Characteristics in Chenzhou, China

Yaping Chen ¹, Bohong Zheng ^{1,*} and Yinze Hu ²

¹ Architecture and Art School, Central South University, Changsha 410075, China; 171301014@csu.edu.cn

² Business School, Hunan University, Changsha 410082, China; huyinze@hnu.edu.cn

* Correspondence: zhengbohong@csu.edu.cn

Received: 13 March 2020; Accepted: 6 April 2020; Published: 8 April 2020



Abstract: The local climate zone (LCZ) has become a new tool for urban heat island research. Taking Chenzhou as the research object, eight urban spatial form elements and land cover elements are calculated respectively through ArcGIS, Skyhelios and ENVI software. The calculation results are then rasterized and clustered in ArcGIS to obtain the LCZ map at a resolution of 200 m. Afterwards, the land surface temperature (LST) of different local climate zones in the four seasons from 2017 to 2018 is further analyzed using one-way ANOVA F-test and Student's *t*-test. The results suggest that: (1) by adding localized LCZ classes and applying the semi-automatic algorithm on the Arc-GIS platform, the final overall accuracy reaches 69.54%, with a kappa value of 0.67, (2) the compact middle-rise buildings (LCZ-2') and open low-rise buildings (LCZ-6) heavily contribute to the high LST of the downtown area, while the large low-rise buildings (LCZ-8) cause the high LST regions in the eastern part of the town, (3) obvious land surface temperature differences can be detected in four seasons among different LCZ classes, with high LST in summer and autumn. Built-up LCZ classes generally revealed higher LSTs than land cover LCZs in all seasons. The findings of this study provide better understandings of the relationship between LCZ and LST, as well as important insights for urban planners on urban heat mitigation.

Keywords: sustainability; local climate zones; ArcGIS; remote sensing; LST retrieval; Chenzhou

1. Introduction

Consistent urbanization leads to the conversion of natural land surface covers using impervious surfaces, which in turn causes an increase of artificial heat emissions. As a result of urbanization, urban areas exhibit significantly higher surface and air temperatures than nearby suburban and rural areas, resulting in the urban heat island (UHI) phenomenon [1], which affects people's health and the sustainable development of cities [2,3]. A number of studies have attempted to achieve an understanding of the interactions between urbanization and UHI [4–9]. One of the most frequent topics is to evaluate the relationship between the urban physical properties and the UHI intensity. Rizwan pointed out that huge quantities of solar radiations are mainly stored and re-radiated in urban areas due to the massive construction materials used and the decreased sky view factor [10]. Morini found that an increase of albedo leads to a decrease of urban temperatures during daytime and in general also at night time, and the temperature may be increased by 1 °C in a few points of the domain when the average albedo of urban areas has been increased from 0.2 to 0.65, 0.6 and 0.45 for roofs, walls and roads, respectively [11]. Lima pointed out that buildings' geometry can affect their energy consumption, while reductions in the thermal load of 16–18% were observed when the urban environment was considered in energy simulations [12]. Chen concluded that both the spatial

configuration of tree canopies and the vertical structure of tree canopies are important predictors for reducing land surface temperature (LST) during daytime and nighttime [13]. Also, specific urban structures and morphologies produce distinct microclimates [14–18], which means that in order to achieve effective urban heat island mitigation, it is necessary to understand and apply urban climatic information in urban planning. However, investigating the impacts of urban physical characteristics on microclimate is a difficult task because of the complexity and variety of land cover, surface structures, construction materials and human activities [19].

In this context, the concept of Local Climate Zones (LCZs), which refers to the classification of urban regions with similar climates, overcomes research limitations. The LCZ class concept is a standardized description of the urban morphology, land cover, building materials, and human activities. The standard local climatic zone scheme includes two main categories: built-up classes and land cover classes. Built-up LCZs include 10 basic classes (LCZ-1–10), which are categorized by compactness of the building layout, building height, building materials and human activities. The land cover LCZs have 7 types (LCZ-A-G) that are classified by their vegetation density and height [19]. Under the LCZ scheme, the UHI effect is no longer regarded as a simple “urban-rural” difference ($\Delta T_{\text{urban-suburb}}$), but rather a temperature difference between LCZs ($\Delta T_{\text{LCZx-y}}$) [20]. Such a definition makes the LCZ methodology a universally comparable approach for urban microclimatology studies, and facilitates knowledge transfer between urban climatologists, planners and practitioners [19]. Among the LCZ-based UHI studies, urban thermal statistics are generated by stationary measurements (e.g., from meteorological stations and the HOBO-Logger) [21,22], mobile measurements (e.g., automobile traverses) [23,24], numerical simulation data (e.g., temperatures from ENVI-met software and the SOLWEIG model) [17,25] and LSTs from remote sensed satellite data [26–28].

Since Steward and Oke formally proposed the concept of the local climate zone in 2012 [19], the amount of related research has increased. The investigations on LCZ mapping and the correlation between LCZ patterns and the urban heat island distribution are the focus of much attention at present. There are two primary methods to realize local climate zone mapping, which are the GIS-based method and [29–31] the WUDAPT method (World Urban Database and Access Portal Tools) [32–34]. For GIS-based classification, the urban 3D building database, 2D road database and remotely sensed reflectance information are needed for input data, and the LCZ classification generally comprises calculation and clustering steps. Meanwhile, the LCZ classification based on the WUDAPT method only needs remote sensing data, which is available on the Google Earth platform, and SAGA GIS software. This method processes mapping automatically and generates vector results [27]. Even though the input data for the GIS method is difficult to acquire and the classification process is rather complex, it is more accurate than the WUDAPT method because it relies on precise GIS data on the urban morphology, planning and even building information to calculate each contributing factor for classifying LCZs [34], while the WUDAPT method is a machine learning algorithm, which depends on the number and quality of training samples and remote sensing images used [35,36].

Nowadays, various countries around the world have applied the LCZ concept to classify urban morphology, mostly focused on the high-density metropolitan areas. However, as a universal classification method for local climate, more cities should be included and the classification accuracy still needs to be improved. Additionally, most of the recent research was only conducted during the summer season, while little consideration was provided for the seasonal characteristics of LCZ classes. In this study, we map the LCZs of Chenzhou city in China, with the following purposes: (1) to classify LCZs more accurately using an improved GIS method, (2) to investigate the relationship between land surface temperature (LST) and LCZ classes in all four seasons.

2. Materials and Methods

2.1. Study Area

Chenzhou is located in southern China and the southeast region of Hunan Province, with the longitude $112^{\circ}13'–114^{\circ}14'$ E and the latitude $24^{\circ}53'–26^{\circ}50'$ N (Figure 1). The total administrative area is $19,317\text{ km}^2$. It has a subtropical monsoon humid climate, with a long summer heat period and a short winter cold period. Our study is focus on the central city area, which is 160 km^2 , including the east and west town areas. The urban construction land is 103.36 km^2 according to the master planning department of Chenzhou.

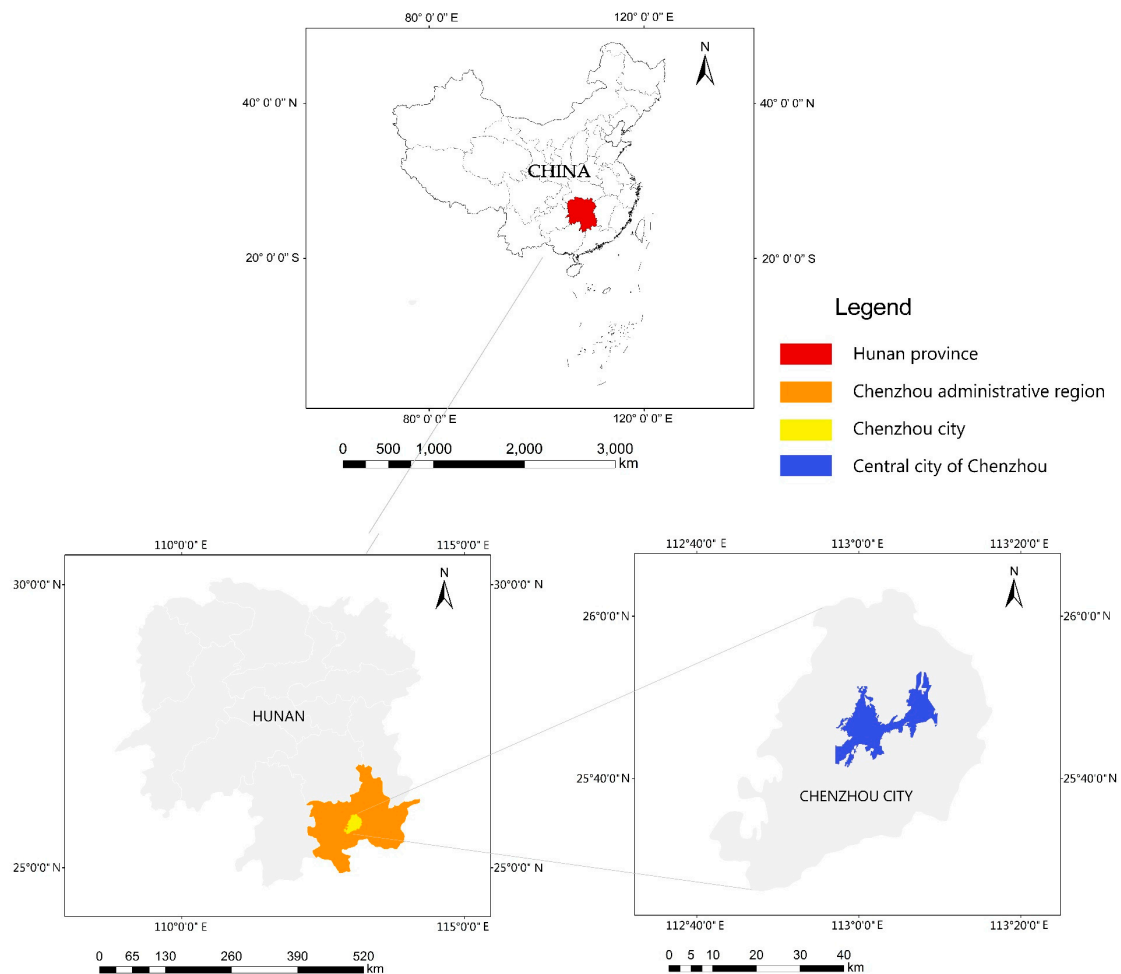


Figure 1. The location of Chenzhou city.

2.2. Data

The workflow of LCZ mapping is illustrated in Figure 2. Landsat 8 remote sensing images, building data and land use data are used as the input data. The output data are LCZ indicators such as the building height (BH), building surface fraction (BSF), sky view factor (SVF), street aspect ratio (SAR), terrain roughness (TR), vegetation coverage ratio (VCR), impervious surface fraction (ISF) and pervious surface fraction (PSF). Other urban planning information was collected from the planning department of Chenzhou, which included the building data, street data and land use data. The building footprint and building height were collected from the building data, and street cover data in polygon were received from the street data. The urban and rural land use information were collected from the land use data.

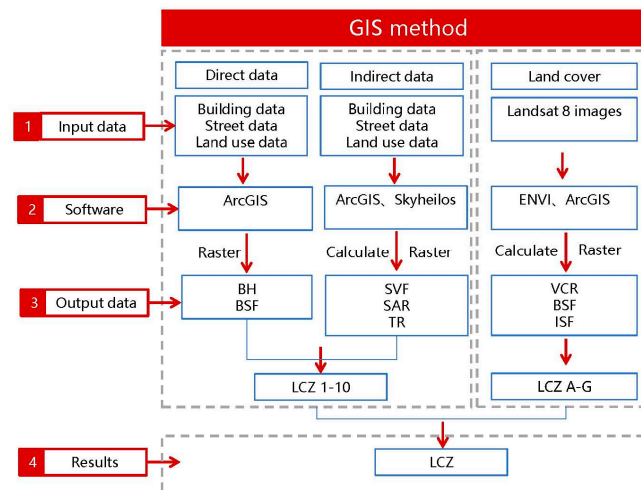


Figure 2. ArcGIS-based local climate zone classification workflow.

2.3. Methods

2.3.1. Local Climatic Zone Mapping

Local climate zone has been commonly defined and classified using blocks [37] or fixed size grids [38]. The former is related to the shape, scale and land use of the block, while the latter divides the urban texture evenly, avoiding the errors caused by the different sizes and uses of land. For the latter, the grid size should first be determined in order to ensure the classification accuracy, which is already discussed in the previous studies [18,35]. The more even the building height is within the grid, the more appropriate the grid size is. By building a semi variogram model in ArcGIS, the height range of the strong autocorrelation of buildings was obtained. As can be seen from Figure 3, the building in the main urban area of Chenzhou indicates a stable building height at a distance of 167.22 m (dash line), thus the grid size was set at 200×200 m. Then, the LCZ indicators were calculated using different methods (Table 1). Finally, after visualizing eight indicators in ArcGIS (Figure 4), the clustering rules were made according to the indicator range to generate the LCZ map.

1. Spatial form elements

Average building height (BH) and building surface fraction (BSF) were calculated directly in ArcGIS based on the building data (Figure 4a,b). However, indirect spatial form elements needed to be calculated by using multiple steps: (1) The sky view factor values were extracted at every 200 m using Skyhelios software and then rasterized in ArcGIS (Figure 4c,d). (2) Calculating the SAR (street aspect ratio) of streets required the following steps: Firstly, we found out the total covered area of streets, then, we divided the total covered area by the total length of the same streets to achieve the average width. Finally, we worked out the SAR by dividing the average height of buildings along the streets by the average width (Figure 4e,f) [29]. (3) The calculation of terrain roughness (TR) was based primarily on the Davenport classification (Table 2) [39]. According to the expression of roughness grades 4, 5 and 6, the rough and very rough grid cells were categorized according to the building height and building surface fraction index in ArcGIS. Then other roughness grades were manually selected according to the representative morphology (Figure 4g).

2. Land cover elements

Land cover elements of LCZs include the vegetation coverage ratio (VCR), impervious surface fraction (ISF) and pervious surface fraction (PSF). The vegetation coverage ratio is obtained by obtaining remote sensing images through ENVI software (Figure 4h,i). Due to the large number of unbuilt areas which are presented as bare soil (LCZ-F), the ISF cannot be simply calculated using the formula “ISF

= 1 - (BSF + VCR)" as in a high-density city [29]; instead, the ISF needs to be obtained using linear spectral mixing model in ENVI. In that case, the radiometric correction and principal component analysis (MNF) of the cropped image were firstly used to select the end element of the two-dimensional scatter map, which was used as the region of interest for the mixed linear spectral decomposition. Then, the generated high albedo percentage image and the low albedo percentage image were added to obtain the preliminary impervious layer. After the vegetation and the water body were masked, the ISF vector and raster maps (Figure 4j,k) were obtained with the threshold (0, 1]. Finally, PSF was calculated using the formula "PSF = 1 - ISF".

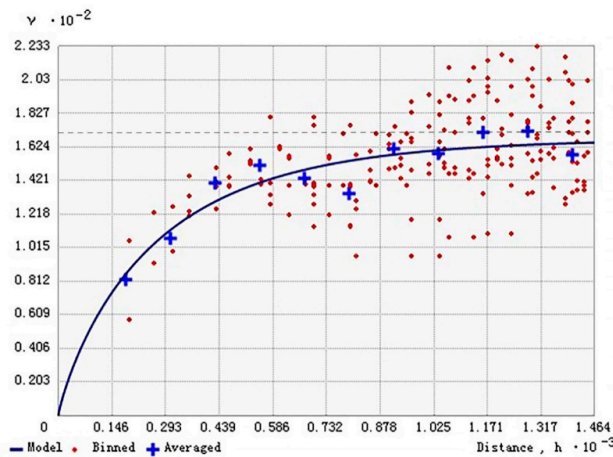


Figure 3. Semi-variogram of building height in Chenzhou.

Table 1. Data and calculation method for local climate zone (LCZ) indicators.

Indicators	Data	Calculation
BH	Building Data	BH = Sum of building height/building number
BSF	Building Data	BSF = building area/building number
SVF	Building Data	SVF = Sum of SVF/Number of measuring points
SAR	Building and road data	Average street width = Street area/street length SAR = Average building height/Average street width
TR	Building and Landsat 8	Davenport classification
VCR	Landsat 8	ENVI
ISF	Landsat 8	ENVI
PSF	Landsat 8	Perviousness = 1 - Imperviousness

Table 2. Davenport standard roughness classification (2000 Edition) [38].

Roughness Grade	Z0(m)	Type	Representative Form
1	0.0002	sea level	Open sea and lake, snow plain, flat desert, tarmac, etc.
2	0.005	smooth	Beach, marsh, frozen water, snow, etc.
3	0.03	open	Low plants, grazing grass, airstrips, etc.
4	0.10	Relative open	Agricultural areas with low plants (crops), open rural areas, suburban open residential areas that are relatively separated and spaced at least 20 times the building height
5	0.25	rough	Buildings with tall plants (crops), scattered and spaced 8 to 12 times the building height
6	0.5	Very rough	Jungle, orchard, grove, low-rise building with no more than 3 to 7 times space
7	1.0	smooth	Mature and regular forests, high-density built-up areas and small changes in building height
8	≥2	chaos	Mixed low-rise and high-rise buildings in urban centers, large areas of forests, mixed areas of irregular height and open space

3. Clustering Rules

Afterwards, output data above were overlaid and clustered in the ArcGIS software platform. In the first step, the built-up LCZs and the land cover LCZs were classified based on their BSF. When the

BSF was greater than 10%, it was classified as a built-up LCZ. If the building surface fraction was less than 10%, it belonged to the land cover LCZs. In the second step, the built-up classes LCZ-1, LCZ-2, LCZ-2', LCZ-3, LCZ-4 and LCZ-5 were further distinguished by their BSF, ISF and BH, as can be seen in Equation (1). Then the SVF, SAR and VCR were used to distinguish the built-up LCZ-6, LCZ-7, LCZ-8, LCZ-8B and LCZ-9, as can be seen in Equation (2). The third step was to further differentiate the land cover LCZ-E and LCZ-G using ISF, as can be seen in Equation (3), and then to use VCR and TR to divide the LCZ-A, LCZ-B, LCZ-C, LCZ-D and LCZ-F, as can be seen in Equation (4).

$$\text{If } ([BH] > w \text{ and } [BSF] > x \text{ and } [ISF] > y) \text{ Then Classify} = \text{“LCZ } z\text{”}, \quad (1)$$

$$\text{elseif } ([SVF] > w \text{ and } [SAR] > x \text{ and } [VCR] > y) \text{ Then Classify} = \text{“LCZ } z\text{”}, \quad (2)$$

$$\text{elseif } ([ISF] < x) \text{ Then classify} = \text{“LCZ } z\text{”}, \quad (3)$$

$$\text{elseif } ([VCR] > w \text{ and } [TR] = x) \text{ Then classify} = \text{“LCZ } z\text{”}. \quad (4)$$

Here, w , x and y refer to the corresponding indicator value, while z represents the LCZ type distinguished in the step.

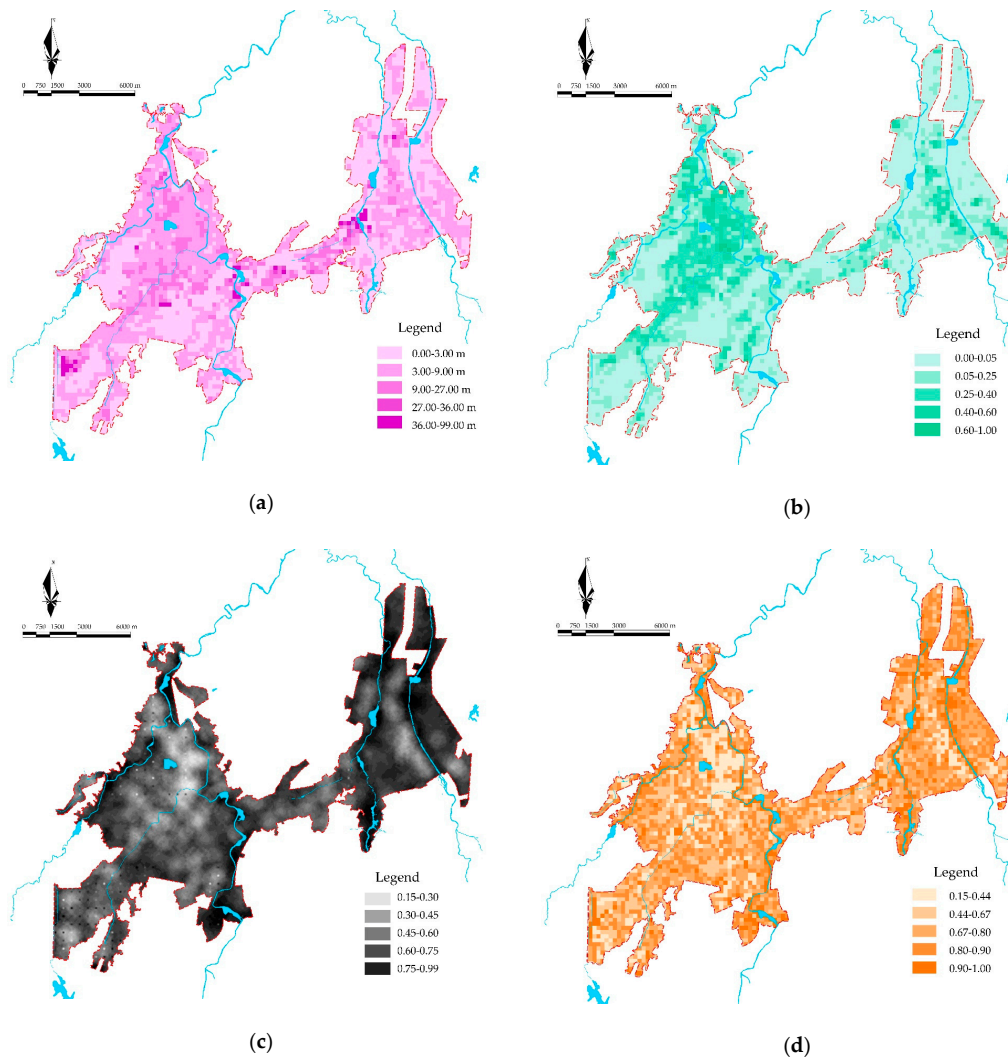


Figure 4. Cont.

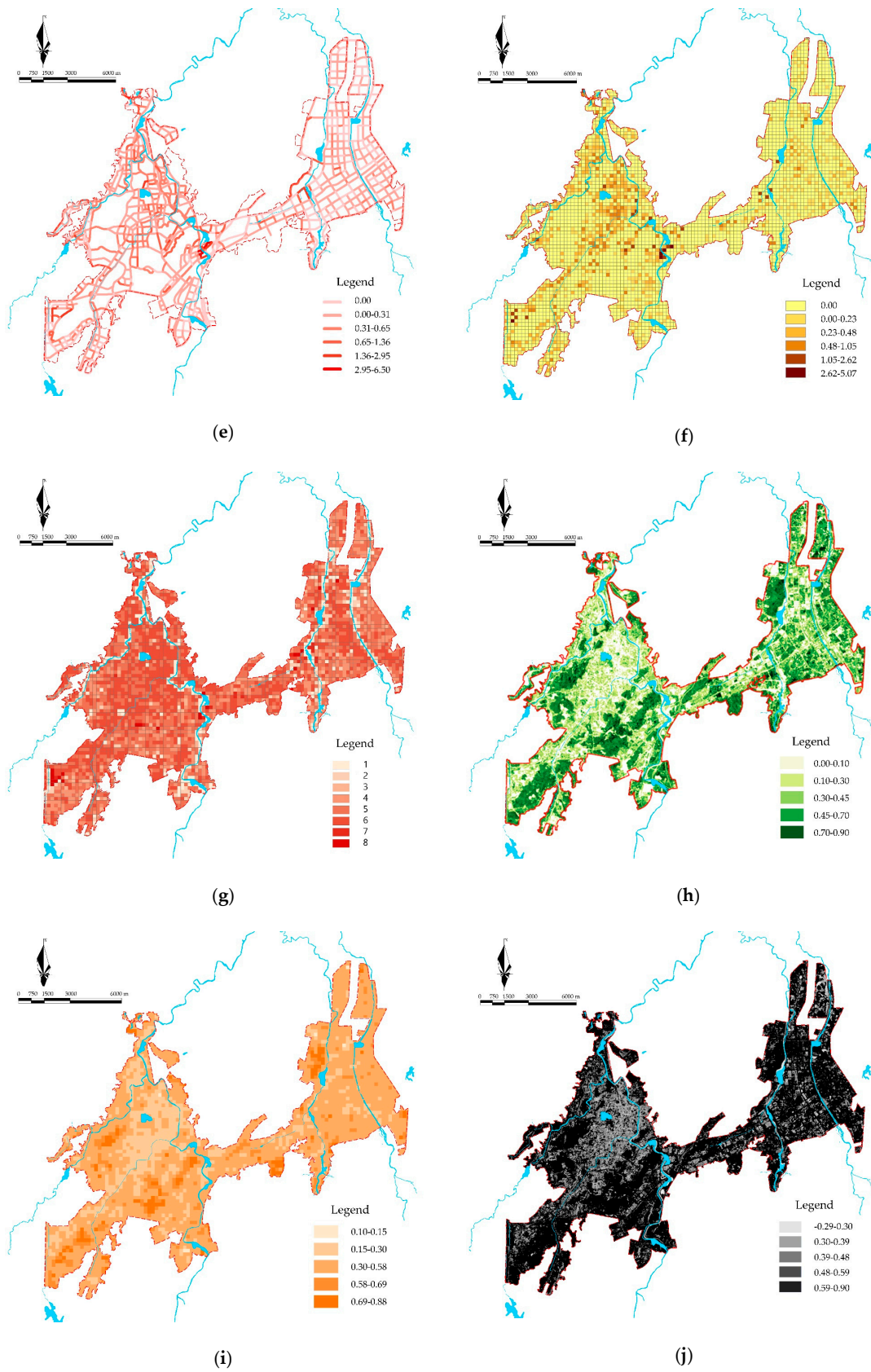


Figure 4. Cont.

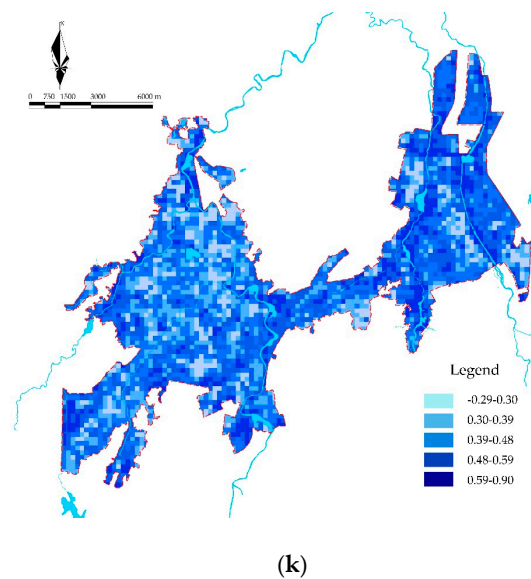


Figure 4. (a) Average building height raster map; (b) Average building surface fraction raster map; (c) Sky view factor vector map, (d) Sky view factor raster map; (e) Street aspect ratio vector map; (f) Street aspect ratio raster map; (g) Terrain roughness raster map; (h) Vegetation coverage rate vector map; (i) Vegetation index vector map; (j) Impervious surface fraction vector map; (k) Impervious surface fraction raster map.

2.3.2. Seasonal Variation Characteristics of Land Surface Temperature in LCZ

The LSTs for all four seasons were obtained to further investigate the relationships between local climate zone and land surface temperature. First of all, remote sensing images with less cloud cover from 2017 to 2018 were selected (Table 3) in order to retrieve the land surface temperature. Secondly, the seasonal differences of paired LCZ classes were analyzed using a one-way ANOVA F-test (Tukey), with “ $p < 0.05$ ” indicating that the difference was significant. Finally, the temperature differences between standard LCZs and sub-class LCZs were analyzed by using the Student’s t -test.

Table 3. Landsat 8 remote sensing images of four seasons during 2018–2018 in Chenzhou.

Season	Data	Date	Cloud
Spring	Landsat 8	2018-04-08	1.3
Summer	Landsat 8	2017-07-26	15.08
Autumn	Landsat 8	2017-10-30	6.36
Winter	Landsat 8	2018-02-03	13.7

3. Results

3.1. Localize the Local Climate Zone Class

According to the building data of Chenzhou, 76.11% of the total buildings are low-rises (1–3 floors), while multi-floor (4–6 floors) and middle-rise (7–11 floors) buildings account for 8.06% and 4.62% of total buildings, respectively, which are dominant in the city core. As such, some localized changes to the LCZ should be made in accordance with Chenzhou’s current situation. Firstly, it is necessary to add LCZ-2’ in addition to LCZ-2. On the one hand, the building height of standard LCZ-2 (12–18 m) cannot properly describe newly built buildings in Chenzhou because most of them are over 18 m. On the other hand, it is generally known that the building height has influence over air temperature and wind velocity [39], and therefore any misclassification may also affect future climate analysis. Secondly, even though low rise buildings are very common in Chenzhou, it is noticeable that the city is currently in the process of urban renewal, where some of the low-rise buildings are

being replaced by high-rise buildings, especially in the early developed downtown area. Therefore, the mixing class LCZ-34 (compact low-rise and high-rise mixed) was added. Since most of the industrial regions in Chenzhou are covered with greenery, the large and low-rise buildings mixed with vegetation (LCZ-8B) has also been added (Table 4). Finally, LCZ-10 (heavy industry) was deleted because there is no heavy industry within the study boundary.

Table 4. LCZ classes and indicators in Chenzhou.

	Standard LCZ Class			New LCZ Class
Built-up LCZ	LCZ-1 Compact high-rise BH: ≥ 36 m BSF: 40–60% SVF: 0.2–0.4 SAR: > 2 ISF: 40–60% PSF: $< 10\%$ VCR: $< 10\%$ TR: 8	LCZ-2 Compact multi-floor BH: 12–18 m BSF: 40–70% SVF: 0.3–0.6 SAR: 0.75–2 ISF: 30–50% PSF: $< 20\%$ VCR: $< 20\%$ TR: 6–7	LCZ-3 Compact low-rise BH: 3–9 m BSF: 40–70% SVF: 0.2–0.6 SAR: 0.75–1.5 ISF: 20–50% PSF: $< 30\%$ VCR: $< 30\%$ TR: 6	LCZ-2' Compact middle-rise BH: 14–33 m BSF: 40–70% SVF: 0.3–0.6 SAR: 0.75–2 ISF: 30–50% PSF: $< 20\%$ VCR: $< 20\%$ TR: 6–7
	LCZ-4 Open high-rise BH: > 36 m BSF: 20–40% SVF: 0.5–0.7 SAR: 0.75–1.25 ISF: 30–40% PSF: 30–40% VCR: 30–40% TR: 7–8	LCZ-5 Open middle-rise BH: 12–18 m BSF: 20–40% SVF: 0.5–0.8 SAR: 0.3–0.75 ISF: 30–50% PSF: 20–40% VCR: 20–40% TR: 5–6	LCZ-6 Open low-rise BH: 3–9 m BSF: 20–40% SVF: 0.6–0.9 SAR: 0.3–0.75 ISF: 20–50% PSF: 30–60% VCR: 30–60% TR: 5–6	LCZ-34 Compact low-middle-rise mixed BH: 3–33 m BSF: 40–70% SVF: 0.3–0.6 SAR: 0.75–2 ISF: 30–40% PSF: 30–40% VCR: 30–40% TR: 7–8
	LCZ-7 Lightweight low-rise BH: 3–9 m BSF: 60–90% SVF: 0.2–0.5 SAR: 1–2 ISF: $< 20\%$ PSF: $< 30\%$ VCR: $< 30\%$ TR: 4–5	LCZ-8 Large low-rise BH: 3–9 m BSF: 30–50% SVF: > 0.7 SAR: 0.1–0.3 ISF: 40–50% PSF: $< 20\%$ VCR: $< 20\%$ TR: 5	LCZ-9 Sparsely built BH: 3–9 m BSF: 10–20% SVF: > 0.8 SAR: 0.1–0.25 ISF: $< 20\%$ PSF: 60–80% VCR: 60–80% TR: 5–6	LCZ-8B Large low-rise mixed with plant BH: 3–9 m BSF: 30–50% SVF: > 0.6 SAR: 0.1–0.3 ISF: 40–50% PSF: 20–40% VCR: $< 20\%$ TR: 5
Land cover LCZ	LCZ-A Dense trees ISF: $< 10\%$ PSF: $> 90\%$ TR: 8 VCR: $> 90\%$ BSF: $< 10\%$	LCZ-B Scattered trees ISF: $< 10\%$ PSF: $> 90\%$ TR: 5–6 VCR: $> 90\%$ BSF: $< 10\%$	LCZ-C Scrub ISF: $< 10\%$ PSF: $> 90\%$ TR: 4–5 VCR: $> 90\%$ BSF: $< 10\%$	LCZ-D Low plants ISF: $< 10\%$ PSF: $> 90\%$ TR: 3–4 VCR: $> 90\%$ BSF: $< 10\%$
	LCZ-E Bare paved ISF: $> 90\%$ PSF: $< 10\%$ TR: 1–2 VCR: $< 10\%$ BSF: $> 90\%$	LCZ-F Bare soil ISF: $< 10\%$ PSF: $> 90\%$ TR: 1–2 VCR: $< 10\%$ BSF: $< 10\%$	LCZ-G Water ISF: $< 10\%$ PSF: $> 90\%$ TR: 1 VCR: $< 10\%$ BSF: $< 10\%$	

3.2. Accuracy Assessment

A Confusion matrix is an effective tool to evaluate the LCZ classification model [27,40] where each column represents the predicted results, and each row represents the real situation of the sample. Standard accuracy measures were calculated using the confusion matrix including: the overall accuracy (OA), which is the percentage of correct classifications; producer accuracy (PA), which is the percentage of correct classifications of the reference class; user accuracy (UA), which refers to the percentage of the pixels classified as class X that actually belongs to this class; and the κ -estimate, which summarizes different accuracies in a single measure. For this study, 8% (877 grids) of the sample were randomly selected to test the classification results in Chenzhou (Table 5).

Table 5. The accuracy test of local climate zone in Chenzhou based on the confusion matrix.

		Reference Data																		User Accuracy (%)	User Accuracy Variance	
		LCZ-1	LCZ-2	LCZ-2'	LCZ-3	LCZ-3A	LCZ-4	LCZ-5	LCZ-6	LCZ-7	LCZ-8	LCZ-8B	LCZ-9	LCZ-A	LCZ-B	LCZ-C	LCZ-D	LCZ-E	LCZ-F			LCZ-G
Classification Data	LCZ-1	5	2	0	0	1	1	0	0	0	0	0	0	0	0	0	0	1	0	0	50.00	0.33
	LCZ-2	2	32	9	0	6	1	0	0	1	0	0	0	0	0	0	0	0	0	0	62.75	0.13
	LCZ-2'	0	9	18	4	0	0	0	0	0	0	1	0	0	0	0	0	0	0	0	56.25	0.17
	LCZ-3	2	1	5	53	3	0	0	12	0	0	0	1	0	0	0	0	0	0	1	67.95	0.10
	LCZ-3A	1	1	0	3	11	0	5	0	0	0	0	1	0	0	2	0	0	0	0	45.83	0.20
	LCZ-4	2	0	0	0	0	12	3	0	0	0	0	0	0	0	1	0	0	0	0	66.67	0.22
	LCZ-5	0	0	0	0	4	0	25	0	0	0	1	0	0	1	3	0	0	0	1	71.43	0.15
	LCZ-6	0	1	0	3	0	0	0	68	0	0	0	0	1	1	3	5	0	0	1	81.93	0.08
	LCZ-7	0	0	0	1	0	0	0	4	21	0	0	0	0	0	2	2	0	0	0	70.00	0.17
	LCZ-8	0	0	0	0	0	1	0	1	0	5	1	0	0	0	0	0	1	0	0	55.56	0.34
	LCZ-8B	0	1	0	0	0	0	0	6	0	3	47	2	0	0	1	2	1	0	0	74.60	0.11
	LCZ-9	0	0	0	0	0	0	2	4	0	0	2	72	0	7	16	6	1	0	0	65.45	0.09
	LCZ-A	0	1	0	0	0	0	0	0	0	0	0	0	3	1	1	0	0	0	0	50.00	0.44
	LCZ-B	0	0	0	0	0	0	3	4	1	1	0	0	2	50	24	7	0	0	0	54.35	0.10
	LCZ-C	0	0	0	1	0	0	0	0	0	0	0	0	14	21	82	5	0	0	0	66.67	0.08
	LCZ-D	0	0	1	0	2	0	1	0	1	0	0	0	4	1	3	43	0	0	0	76.79	0.11
	LCZ-E	0	0	0	0	0	0	0	0	0	0	0	0	0	0	0	0	4	1	0	80.00	0.39
LCZ-F	0	0	1	0	0	1	0	0	0	0	0	0	0	1	0	1	1	27	0	84.38	0.13	
LCZ-G	0	0	0	1	0	0	0	3	1	0	0	0	0	0	0	0	0	1	12	66.67	0.22	
Weights	10	51	32	78	24	18	35	83	30	9	63	110	6	92	123	56	5	32	18			
Producer Accuracy (%)	41.67	66.67	52.94	80.30	40.74	75.00	64.10	66.67	84.00	55.56	90.38	94.74	12.50	60.24	59.42	60.56	44.44	93.10	80.00			
Producer Accuracy Variance	0.24	0.11	0.14	0.09	0.16	0.19	0.12	0.07	0.14	0.28	0.08	0.05	0.11	0.09	0.07	0.09	0.25	0.09	0.19			
Portmanteau Accuracy (%)	98.63	96.00	96.57	95.66	96.69	98.86	97.26	94.40	98.51	99.09	97.60	95.20	97.26	91.43	88.91	95.31	99.31	99.20	98.97			
Portmanteau Accuracy Partial (%)	29.41	47.76	37.50	58.24	27.50	54.55	51.02	58.12	61.76	38.46	69.12	63.16	11.11	40.00	45.81	51.19	40.00	79.41	57.14			
Overall Accuracy Kappa																			67.31% 0.65			

It is found in Table 5 that the accurately detected classes are open building areas such as LCZ 4 (66.67%), LCZ-5 (71.43%) and LCZ-6 (81.93%), which are the main LCZ classes in Chenzhou. Also, the newly add class LCZ-8B, as well as the LCZ-E and LCZ-F have high accuracies of 74.60%, 80.00% and 84.38%, respectively. However, there are still some misclassifications with low UA values in LCZ-1, LCZ-34, LCZ-A and LCZ-B. We determined by checking the results of LCZ classes' spatial distribution patterns with the actual urban morphology of Chenzhou that the compact high-rise buildings (LCZ-1) have significant errors (50%) due to some LCZ-1 regions having been misclassified into compact mid-rise building class (LCZ-2'). However, since LCZ-1 only takes up 1.03% of Chenzhou, its influence on OA is insignificant. Additionally, the land cover classes LCZ-A (50.00%), LCZ-B (54.35%) and LCZ-C (66.67%) tend to be confused with each other, which is because the vegetation cover index of remote sensing images better reflect the vegetation density rather than the vegetation height. It was also noted that the accuracy of the mixing class LCZ-34 is the lowest (45.83%), which was attributed to the fact that average building height within the 200×200 m range is easily confused with the parameter value of LCZ-5. In order to minimize the errors caused by the cluster process and have better accuracy results, one more step was added to distinguish LCZ-34 (buildings of 3–33 m) with LCZ-5 (buildings of 12–15 m), which was to examine the standard deviation of building height in each 200×200 m grid in ArcGIS. In that case, grids with average BH value more than one standard deviation above the average BH mean were defined as LCZ-34, and areas with BH value less than one standard deviation below the BH mean were defined as LCZ-5. The final LCZ map was generated and is shown in Figure 5b, with the changes mainly located in three areas of Chenzhou. The UA value of LCZ-34 reached 67.12%, and the overall accuracies increased to 69.54%, with the kappa growing to 0.67 (Table 6).

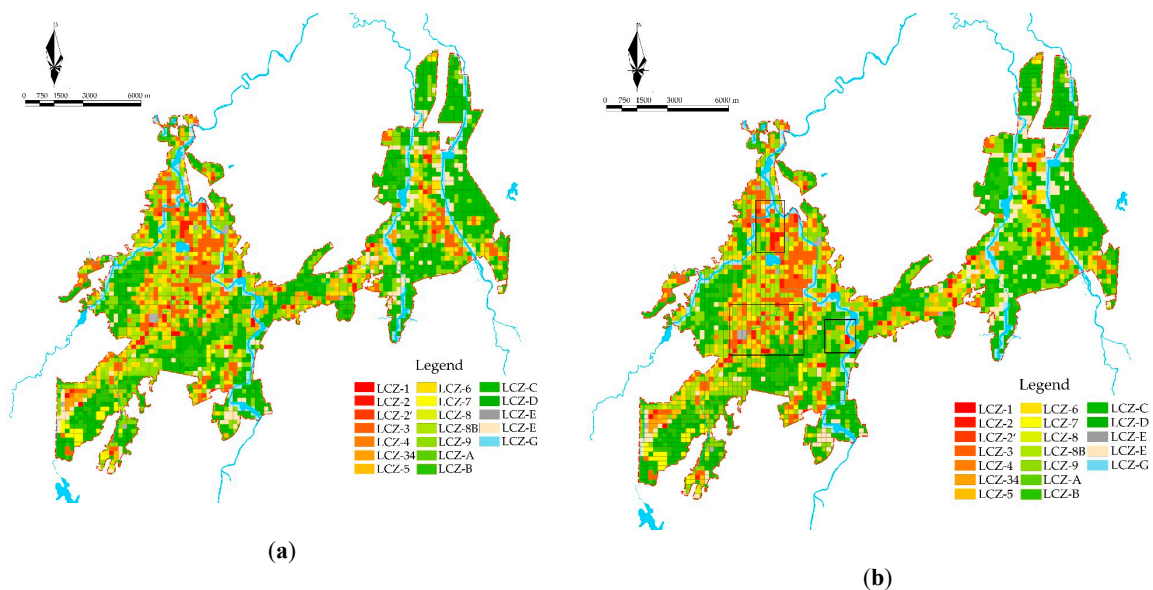


Figure 5. (a) Local climate zone map (Version 1) of Chenzhou; (b) Local climate zone map (Version 2) of Chenzhou, with the changes mainly in the black frames.

Table 6. Comparison of classification accuracy in LCZ map Version 1 and Version 2.

LCZ Map	UA (LCZ-34)	OA	Kappa
Version 1	45.83%	67.31%	0.65
Version 2	67.12%	69.54%	0.67

3.3. LCZ Pattern in Chenzhou

According to the final LCZ map in Figure 5 even though land cover LCZs share an area coverage of 53.37%, which is higher than that of the built-up LCZ (44.63%), LCZ-6 (6.33%), LCZ-2' (3.48%),

LCZ-5 (3.40%) and LCZ-34 (3.12%) are the dominant classes in the center of the city. Another LCZ class that covers a large proportion of land (12.96%) is LCZ-9 (sparsely built area), which is mostly found in suburban areas. Furthermore, the proportion of open building areas (33.64%) is higher than that of compact building areas (10.98%) in terms of the building surface fraction parameter. Regarding the building height, high-rise buildings (LCZ-1 and LCZ-4) account for only 2.03% of Chenzhou's land, while the middle-rise buildings (LCZ-2, LCZ-2' and LCZ-4) and low-rise buildings (LCZ-8B and LCZ-6) are more common in Chenzhou. It is also observed in Figure 5b that the sub-classes LCZ-2' and LCZ-34 are concentrated in the early developed downtown, which mostly covers commercial areas and residential areas. Meanwhile, the LCZ map detects LCZ-8B (4.81%) and LCZ-4 (1.00%) in the industrial district in the east part of Chenzhou. As for land cover LCZs, LCZ-C (shrub) and LCZ-A (dense forest) constitute 17.42% and 14.05%, respectively of the inner urban area, followed by LCZ-B (9.74%) and LCZ-G (4.94%). LCZ-A-C are distributed in two parallel lines in the downtown area, which is well distinguished by built-up LCZs in the city core.

3.4. Analysis of Land Surface Temperature Characteristics in Local Climate Zones

As can be observed in Figure 6, even though land surface temperature varies across the four seasons, it revealed similar spatial distributions of LST in Chenzhou. Except for winter, the warmest temperatures tend to be experienced in the central area of western downtown, where LCZ-2', LCZ 34, LCZ-5 and LCZ-6 have large proportions, as well as the industrial areas (LCZ-8 and LCZ-8B) to the east of Chenzhou in all seasons. In particular, the east town industrial areas experience a large proportion of extreme high LST up to 40.75 °C in the summer; however, the high LST areas of the east town shrink in the autumn. In contrast, LCZ-A, LCZ-B and LCZ-C have comparatively lower LSTs during the four seasons, which are generally 2–4 °C cooler than the built-up LCZs and can be up to 10 °C cooler than the hottest regions in summer.

A boxplot of seasonal LST (Figure 7) in different LCZs was then developed to further investigate their relations. As seen in Figure 7, the mean LSTs of all LCZs are usually the highest in the summer, especially in LCZ-8 (39.2 °C), LCZ-2' (38.3 °C) and LCZ-6 (38.1 °C). LCZ-2 and LCZ-E also contributed largely to the high LST regions. In contrast, the lowest temperatures occur in the land cover classes (LCZ-A, LCZ-B and LCZ-G) and some built-up classes (LCZ-7 and LCZ-9). In the spring, a small LST difference between built-up classes and land cover classes was observed. High LST is only found in LCZ-8 and LCZ-8B with mean values of 29.53 °C and 26.16 °C, respectively. Regarding the autumn season, the quartile ranges and outliers of most LCZs are higher than those in the spring, with high LST found in LCZ-8 (35.06 °C), LCZ-2 (31.73 °C) and LCZ-3 (31.45 °C). Even though the LST in winter is the coolest in all LCZ classes, a similar trend in LCZ has been anticipated, that is, values in built-up LCZ are higher than that of land cover LCZs except for LCZ-E.

The results of one-way ANOVA F-test satisfied the normality and homogeneity of variance. Afterwards, the Tukey analysis was applied and results revealed that most of the paired LCZ types ($p < 0.05$) have statistically significant differences in LST (Figure 8). The normality and homogeneity of variance of each LCZ group was tested by the Kolmogorov-Smirnov test and QQ diagram, with a test level of 0.1. The results of paired LCZ are listed in Figure 8, where the blue grids indicate that there is no significant difference in LST of paired LCZs ($p < 0.05$), while the white grids indicate that differences existed. Overall, the differences between LCZs are statistically significant in most of the LCZ pairs during all the seasons, with the LST values being more distinguishable in the spring and summer. Additionally, the difference between the new LCZs and the original LCZ types (LCZ-8 and LCZ-8B, LCZ-3 and LCZ-34, LCZ-2 and LCZ-2') were further detected using the Student's *t*-test, since it is an important assumption that newly-added LCZs make the classification more accurate and comprehensive. According to the Student's *t*-test results, there are significant LST differences between the paired LCZs. From Table 7, the results confirm that LCZ-8B features a cooler LST than LCZ-8 in all seasons, while the highest difference appears in the summer (3.92 °C), followed by spring and autumn.

Similarly, the LST of LCZ-34 is relatively lower than LCZ-3 seasonally. However, the LST difference between LCZ-2 and LCZ-2' is not significant in the summer and winter.

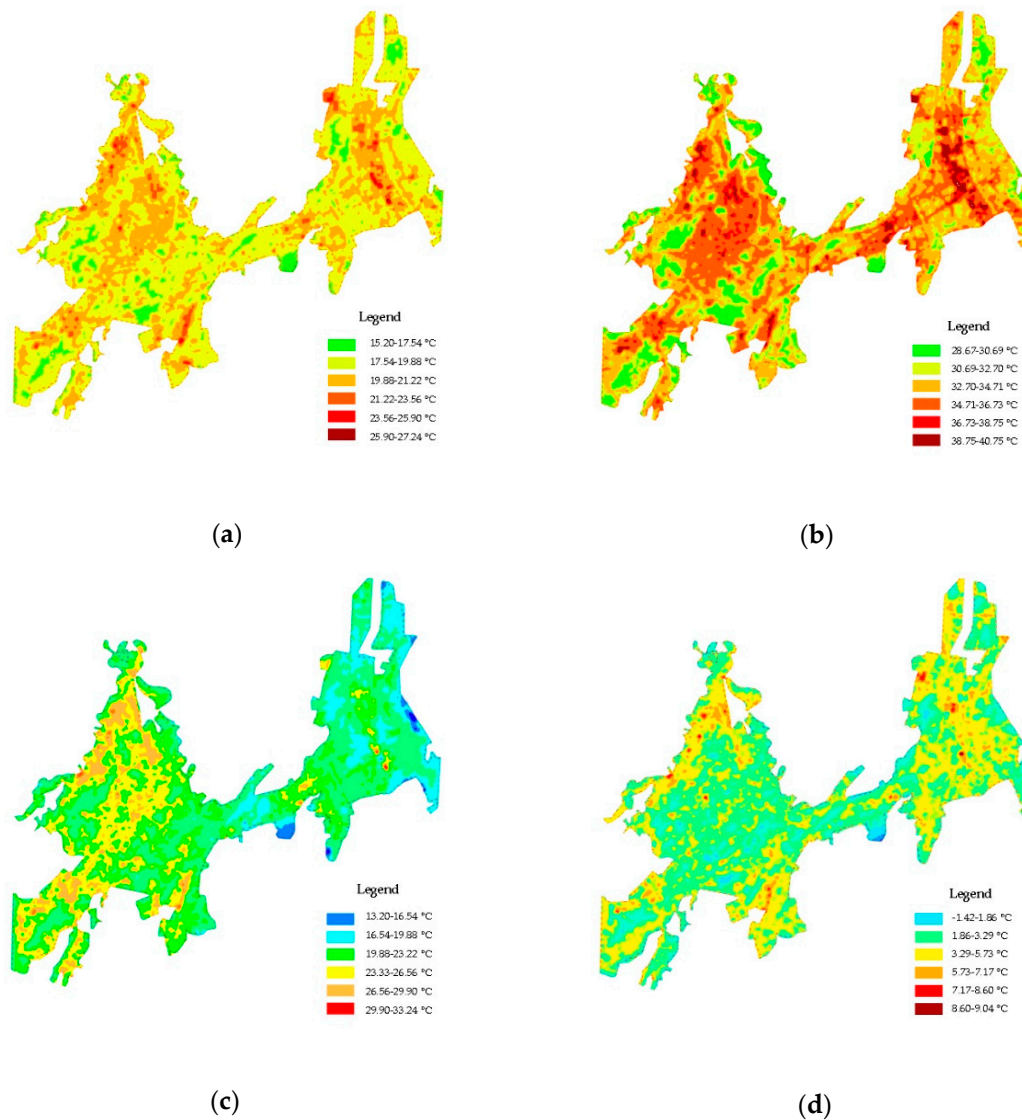


Figure 6. Seasonal land surface temperature in Chenzhou city. (a) Spring; (b) Summer; (c) Autumn; (d) Winter.

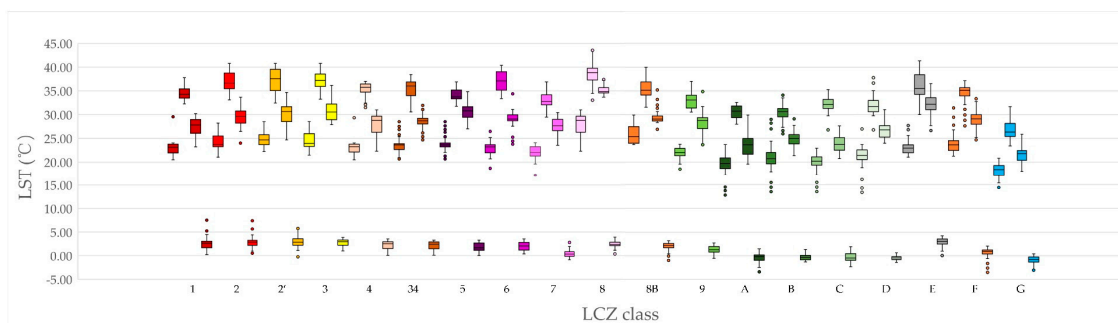


Figure 7. Boxplot of seasonal land surface temperature (LST) in different LCZs. Left to right indicates spring, summer, autumn and winter.

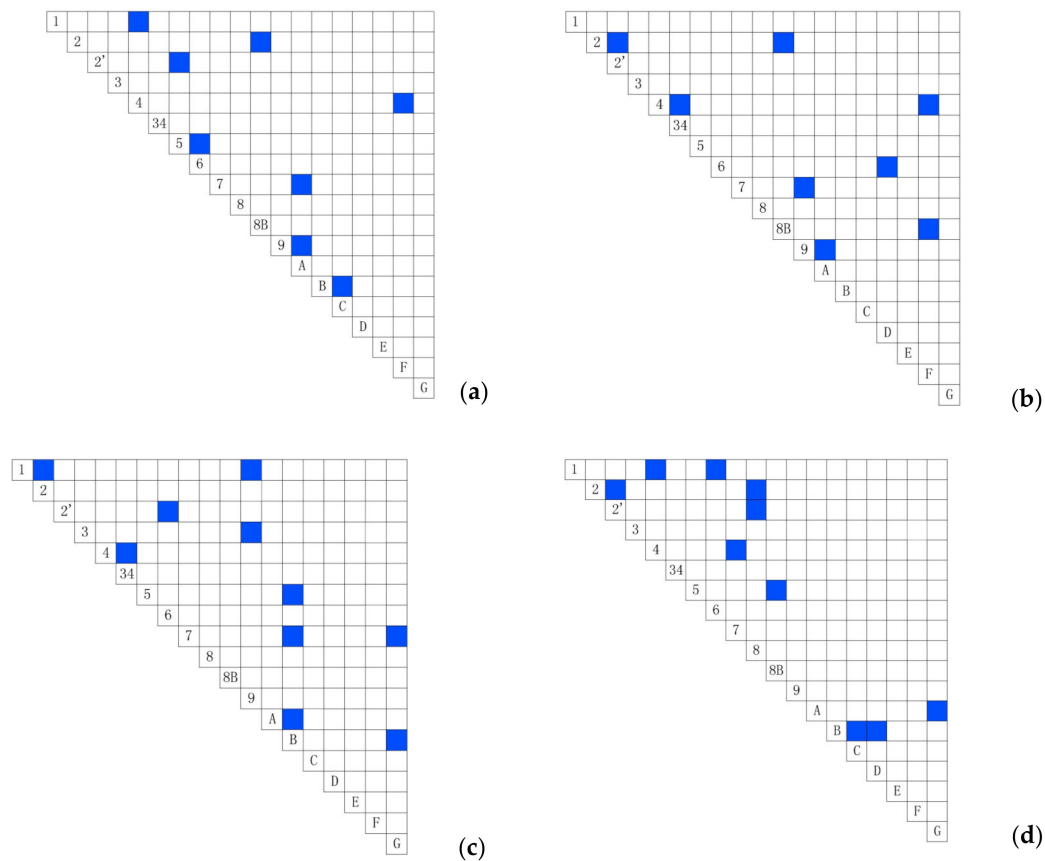


Figure 8. Tukey tests for pairs of LCZ classes during four seasons. (a) Spring; (b) Summer; (c) Autumn; (d) Winter. The blue grid indicates that there is no significant difference in LCZ surface temperature ($p > 0.05$), and the white grid indicates that the LCZ surface temperature is significantly different.

Table 7. Student's t test of LCZ-8 and LCZ-8B, LCZ-3 and LCZ-34, LCZ-2 and LCZ-2'.

Season	Class	Difference	Standard Error of Difference	Lower CL	Upper CL	Significance
Spring	LCZ8-LCZ8B	3.02	0.36	1.33	2.80	0.000
Summer	LCZ8-LCZ8B	3.29	0.39	0.97	2.41	0.000
Autumn	LCZ8-LCZ8B	1.94	0.23	0.73	1.65	0.000
Winter	LCZ8-LCZ8B	1.09	0.13	0.20	0.73	0.000
Spring	LCZ3-LCZ34	3.19	0.38	1.06	2.61	0.000
Summer	LCZ3-LCZ34	2.19	0.26	1.24	2.31	0.000
Autumn	LCZ3-LCZ34	3.27	0.39	2.15	3.74	0.000
Winter	LCZ3-LCZ34	1.17	0.14	0.26	0.83	0.000
Spring	LCZ2-LCZ2'	1.97	0.23	-1.12	-0.16	0.000
Summer	LCZ2-LCZ2'	2.41	0.29	-1.00	0.16	0.073
Autumn	LCZ2-LCZ2'	2.67	0.32	-0.01	1.27	0.000
Winter	LCZ2-LCZ2'	1.60	0.19	-0.67	0.10	0.059

4. Discussion

4.1. The LCZ Classification and LST Characteristics in Chenzhou

Some localized classification steps were adapted to refine the mapping by understanding the LCZ properties in Chenzhou. Firstly, as the optimal resolution of LCZ maps might vary among cities [34], the scale of the grid should be determined first. Unlike the earlier LCZ mapping research focusing on high-density cities [29,33,34], which were usually mapped at a resolution of 300 m, GIS-method classification in a developing city like Chenzhou applied grids of 200×200 m to ensure there was classification accuracy. Secondly, some modifications have been applied to the standard

LCZ classes according to the dominant building forms of Chenzhou, which some previous studies already demonstrated in other countries. For example, a study in Nagpur developed twenty-one LCZ classes, including fourteen standard classes and seven distinct LCZ sub-classes in order to successfully deal with the problems associated with the intermixing of LCZs [25]. Similarly, a study in Colombo, Sri Lanka pointed out that the LCZ approach was not able to capture all of the nuances of urban growth everywhere and therefore a LCZ sub-classification system was needed based on urban spatial particularities [38]. In the current study, the LCZ map of Chenzhou is classified using twelve built-up LCZs and seven land cover LCZs, which includes three new localized LCZ types (LCZ-2', LCZ-34 and LCZ-8B) according to the character of land surface properties. Lastly, even though the Arc-GIS based classification in this study shows high overall accuracy like many other previous research [28,30,37], it detects relatively low accuracies in some LCZ classes, which are mainly in the mixed building types (LCZ-34) and the land cover classes (LCZ-A-C). Although the sub-classification adds complexity to the LCZ map, the misclassifications which occurred in built-up LCZs can be improved by conducting statistical analysis of urban physical structure parameters in the Arc-GIS platform. By examining the standard deviation of building height after classification workflow (Figure 2) in this study, the accuracy of LCZ-34 has been improved from 45.83% to 67.12% and the final LCZ map (Version 2) was generated with higher overall accuracy (69.54%). However, further studies are needed to apply higher resolution satellite images to improve the accuracy of LCZ-A-C.

It was found that some relations existed between the distributions of LCZ and LST. On the whole, for a developing city, the proportion of open building area is larger than that of compact building area, with the open middle-rise regions (LCZ-5) and the open low-rise regions (LCZ-6) appearing with high frequencies. However, the areas with high LST in the city center were mostly compact urban areas (LCZ-2 and LCZ-2') where ventilation was likely to be blocked. Also, high LST regions appear in the eastern industrial zones (LCZ-8 and LCZ-8B) where impervious surfaces have a large proportion. It is generally known that impervious surfaces absorb more solar radiation and emit more long-wave radiation, and thereby leading to higher LST [21,41,42]. Even though the LSTs of the most built-up LCZs exceed that of land cover LCZs, simple low-rise buildings (LCZ-7) and very open lower-rise buildings (LCZ-9), which are common in urban suburbs, exhibit low LST values as well. Similar conclusions were reached in studies of the Yangtze River Delta and Pearl River Delta in China [20,43], and Brno and Prague in Europe [44]. It is also noted that the LCZ-F (bare land) takes up 5.47% of Chenzhou's land, indicating that the unbuilt area of Chenzhou accounts for a significant proportion of its land, which might be attributed to the process of transforming natural environment into an urban environment. Therefore, there is a possibility that the proportion of built-up LCZs in the environment will be larger than that of land cover LCZs in the future. In that case, attention will also need to be paid to LSTs during urban construction, because the LST of LCZ-F reaches 35 °C in the summer.

Generally, the characteristics of land surface temperature in each local climatic zone vary with the seasons, with a high LST in summer, followed by autumn and spring, and the lowest in winter. The LST differences also exist in most LCZ pairs in each season according to the Tukey tests. According to Figures 6 and 7, the highest differences in LSTs are between the built-up LCZ classes during the summer and autumn periods, which means the LSTs might be strongly influenced by LCZ classes during the hot seasons. Moreover, the interpretations of the Student's *t* test suggest that significant LST differences occur between the standard LCZs and the localized LCZ, except for LCZ-2 and LCZ-2'. The mean LST of LCZ-8B is lower than that of LCZ-8, which may due to the fact that the shadows of large low buildings in LCZ-8 are not sufficient to lower the LST, while the vegetation of LCZ-8B (large low-rise with vegetation) produces more shadows and brings soil moisture during the day. Meanwhile, similar results are observed in LCZ-34 when compared to LCZ-3, which might be explained by the shadow of high-rise buildings reducing the radiation temperature [44–46].

4.2. Implementation for Urban Planning

The study of LCZ and LST patterns is beneficial for understanding the land use planning as well as the urban thermal environment. This analysis showed that the key planning areas for mitigating the UHI phenomenon of Chenzhou are LCZ-8 (large low-rise), LCZ-2' (compact middle-rise) and LCZ-6 (open low-rise), which are mainly found in core downtown areas and industrial zones in Chenzhou. Particularly, LCZ-8 and LCZ-2' contribute largely to the hot spots of Chenzhou. Having taken the adverse impacts of these LCZ classes into account, some planning suggestions are made. Firstly, proper greenery should be applied in LCZ-8 areas, which will bring more shadows and surface moisture, as well as cut down the solar radiation in summer. Secondly, it is encouraged to convert compact middle-rise buildings (LCZ-2') to open middle-rise buildings (LCZ-5) or open high-rise buildings (LCZ-4) in central Chenzhou, in order to provide sufficient public space for green areas and to increase urban ventilation. Also, the proper and reasonable distributions of LCZs with lower land surface temperatures such as LCZ-A-C (dense forest, sparse forest and shrub) and LCZ-G (water body) are advisable to mitigate the influence of UHI during the process of urban development

4.3. Limitations

This study aims to map local climate zones in Chenzhou and evaluate its relationship with land surface temperature patterns. However, there are some limitations. The calculation of the surface albedo, surface admittance and anthropogenic heat flux has not been realized. Therefore, it is unknown whether their calculation would have led to a more accurate result. Additionally, even though the accuracy of built-up LCZ classes is improved in this study, satellite data with higher resolutions, as well as other sensors and auxiliary sources such as Open Street Map are still needed in future studies, because the errors of land cover LCZs are possibly due to the spatial resolution of the Landsat data.

5. Conclusions

This paper aims to deepen the knowledge about GIS methods in the LCZ mapping of developing city and further evaluate the four seasons' land surface temperatures in LCZs. In this study, the LCZ scheme has been applied in Chenzhou and a LCZ map has been built using multiple types of software. Meanwhile, the semi-automatic algorithm on the Arc-GIS platform was found to improve mapping efficiency. By providing the sub-classification in Chenzhou, a better understanding of the urban structure, as well as the relations between LCZ map and LST patterns was achieved, which provided important insights for urban planners on urban heat mitigation.

Author Contributions: Conceptualization, Y.C.; methodology, Y.C.; formal analysis, Y.C.; investigation, Y.C. and Y.H.; writing—original draft preparation, Y.C.; writing—review and editing, Y.H.; supervision, B.Z.; funding acquisition, Y.C. and B.Z.; All authors have read and agreed to the published version of the manuscript.

Funding: This research was funded by National Nature Science Foundation of China, grant number 51608535, 31901363; Nature Science Foundation of Hunan Province, China, grant number 2019JJ50990; Fundamental Research Funds for the Central Universities, China, grant number 2018zzts091.

Conflicts of Interest: The authors declare no conflict of interest.

References

1. Voogt, J.A.; Oke, T. Thermal remote sensing of urban climates. *Remote Sens. Environ.* **2003**, *86*, 370–384. [[CrossRef](#)]
2. Farhadi, H.; Faizi, M.; Sanaieian, H. Mitigating the urban heat island in a residential area in Tehran: Investigating the role of vegetation, materials, and orientation of buildings. *Sustain. Cities Soc.* **2019**, *46*, 101448. [[CrossRef](#)]
3. Shahmohamadi, P.; Che-Ani, A.; Eteessam, I.; Maulud, K.N.A.; Tawil, N. Healthy Environment: The Need to Mitigate Urban Heat Island Effects on Human Health. *Procedia Eng.* **2011**, *20*, 61–70. [[CrossRef](#)]

4. Arnfield, A.J. Two decades of urban climate research: A review of turbulence, exchanges of energy and water, and the urban heat island. *Int. J. Clim.* **2003**, *23*, 1–26. [[CrossRef](#)]
5. Giridharan, R.; Ganesan, S.; Lau, S. Daytime urban heat island effect in high-rise and high-density residential developments in Hong Kong. *Energy Build.* **2004**, *36*, 525–534. [[CrossRef](#)]
6. Gago, E.; Roldán, J.; Pacheco-Torres, R.; Ordóñez, J. The city and urban heat islands: A review of strategies to mitigate adverse effects. *Renew. Sustain. Energy Rev.* **2013**, *25*, 749–758. [[CrossRef](#)]
7. Wang, Y.; Akbari, H. Analysis of urban heat island phenomenon and mitigation solutions evaluation for Montreal. *Sustain. Cities Soc.* **2016**, *26*, 438–446. [[CrossRef](#)]
8. Silva, J.S.; Da Silva, R.M.; Santos, C.A.G. Spatiotemporal impact of land use/land cover changes on urban heat islands: A case study of Paço do Lumiar, Brazil. *Build. Environ.* **2018**, *136*, 279–292. [[CrossRef](#)]
9. Yue, W.; Liu, X.; Zhou, Y.; Liu, Y. Impacts of urban configuration on urban heat island: An empirical study in China mega-cities. *Sci. Total. Environ.* **2019**, *671*, 1036–1046. [[CrossRef](#)]
10. Rizwan, A.M.; Dennis, L.Y.; Liu, C. A review on the generation, determination and mitigation of Urban Heat Island. *J. Environ. Sci.* **2008**, *20*, 120–128. [[CrossRef](#)]
11. Morini, E.; Touchaei, A.G.; Rossi, F.; Cotana, F.; Akbari, H. Evaluation of albedo enhancement to mitigate impacts of urban heat island in Rome (Italy) using WRF meteorological model. *Urban Clim.* **2018**, *24*, 551–566. [[CrossRef](#)]
12. Lima, I.; Scalco, V.; Lamberts, R. Estimating the impact of urban densification on high-rise office building cooling loads in a hot and humid climate. *Energy Build.* **2019**, *182*, 30–44. [[CrossRef](#)]
13. Du, X.; Bokel, R.; Dobbela, A.V.D. Spatial configuration, building microclimate and thermal comfort: A modern house case. *Energy Build.* **2019**, *193*, 185–200. [[CrossRef](#)]
14. Wu, Z.; Dou, P.; Chen, L. Comparative and combinative cooling effects of different spatial arrangements of buildings and trees on microclimate. *Sustain. Cities Soc.* **2019**, *51*, 101711. [[CrossRef](#)]
15. Jamei, E.; Rajagopalan, P. Urban development and pedestrian thermal comfort in Melbourne. *Sol. Energy* **2017**, *144*, 681–698. [[CrossRef](#)]
16. Alexander, P.; Fealy, R.; Mills, G. Simulating the impact of urban development pathways on the local climate: A scenario-based analysis in the greater Dublin region, Ireland. *Landsc. Urban Plan.* **2016**, *152*, 72–89. [[CrossRef](#)]
17. Aminipouri, M.; Rayner, D.; Lindberg, F.; Thorsson, S.; Knudby, A.; Zickfeld, K.; Middel, A.; Krayenhoff, E.S. Urban tree planting to maintain outdoor thermal comfort under climate change: The case of Vancouver's local climate zones. *Build. Environ.* **2019**, *158*, 226–236. [[CrossRef](#)]
18. Morini, E.; Castellani, B.; Presciutti, A.; Anderini, E.; Filippini, M.; Nicolini, A.; Rossi, F. Experimental Analysis of the Effect of Geometry and Façade Materials on Urban District's Equivalent Albedo. *Sustainability* **2017**, *9*, 1245. [[CrossRef](#)]
19. Stewart, I.D.; Oke, T.R. Local Climate Zones for Urban Temperature Studies. *Bull. Am. Meteorol. Soc.* **2012**, *93*, 1879–1900. [[CrossRef](#)]
20. Bechtel, B.; Daneke, C. Classification of Local Climate Zones Based on Multiple Earth Observation Data. *IEEE J. Sel. Top. Appl. Earth Obs. Remote Sens.* **2012**, *5*, 1191–1202. [[CrossRef](#)]
21. Quanz, J.A.; Ulrich, S.; Fenner, D.; Holtmann, A.; Eimermacher, J. Micro-Scale Variability of Air Temperature within a Local Climate Zone in Berlin, Germany, during Summer. *Climate* **2018**, *6*, 5. [[CrossRef](#)]
22. Beck, C.; Straub, A.; Breitner, S.; Cyrus, J.; Philipp, A.; Rathmann, J.; Schneider, A.; Wolf, K.; Jacobeit, J. Air temperature characteristics of local climate zones in the Augsburg urban area (Bavaria, southern Germany) under varying synoptic conditions. *Urban Clim.* **2018**, *25*, 152–166. [[CrossRef](#)]
23. Shi, Y.; Lau, K.K.-L.; Ren, C.; Ng, E. Evaluating the local climate zone classification in high-density heterogeneous urban environment using mobile measurement. *Urban Clim.* **2018**, *25*, 167–186. [[CrossRef](#)]
24. Leconte, F.; Bouyer, J.; Claverie, R.; Pétrissans, M. Using Local Climate Zone scheme for UHI assessment: Evaluation of the method using mobile measurements. *Build. Environ.* **2015**, *83*, 39–49. [[CrossRef](#)]
25. Stewart, I.D.; Oke, T.R.; Krayenhoff, E.S. Evaluation of the 'local climate zone' scheme using temperature observations and model simulations. *Int. J. Clim.* **2013**, *34*, 1062–1080. [[CrossRef](#)]
26. Ochola, E.M.; Fakhariadehshirazi, E.; Adimo, A.O.; Mukundi, J.B.; Wesonga, J.M.; Sodoudi, S. Inter-local climate zone differentiation of land surface temperatures for Management of Urban Heat in Nairobi City, Kenya. *Urban Clim.* **2020**, *31*, 100540. [[CrossRef](#)]

27. Cai, M.; Ren, C.; Xu, Y. Investigating the relationship between local climate zone and land surface temperature using an improved WUDAPT methodology—A case study of Yangtze River Delta, China. *Urban Clim.* **2018**, *24*, 485–502. [CrossRef]
28. Geletič, J.; Lehnert, M.; Dobrovolný, P. Land Surface Temperature Differences within Local Climate Zones, Based on Two Central European Cities. *Remote Sens.* **2016**, *8*, 788. [CrossRef]
29. Zheng, Y.; Ren, C.; Xu, Y.; Wang, R.; Ho, J.; Lau, K.K.-L.; Ng, E. GIS-based mapping of Local Climate Zone in the high-density city of Hong Kong. *Urban Clim.* **2018**, *24*, 419–448. [CrossRef]
30. Jan, G.; Michal, L. GIS-based delineation of local climate zones, the case of medium-sized Central European cities. *Morav. Geogr. Rep.* **2016**, *24*, 2–12.
31. Levlovics, E.; Gál, T.; Unger, J. Mapping local climate zones with a vector-based GIS method. *Aerul Și Apa Componente Ale Mediului.* **2013**, 230–423.
32. The World Urban Database and Access Portal Tools. Available online: www.wudapt.org (accessed on 2 October 2019).
33. Ren, C.; Wang, R.; Cai, M. The Accuracy of LCZ maps Generated by the World Urban Database and Access Portal Tools (WUDAPT) Method: A Case Study of Hong Kong. *Urban Heat Island* **2016**, 210–223.
34. Wang, R.; Ren, C.; Xu, Y.; Lau, K.K.-L.; Shi, Y. Mapping the local climate zones of urban areas by GIS-based and WUDAPT methods: A case study of Hong Kong. *Urban Clim.* **2018**, *24*, 567–576. [CrossRef]
35. Bechtel, B.; Alexander, P.; Böhner, J.; Ching, J.; Conrad, O.; Feddema, J.; Mills, G.; Fritz, S.; Stewart, I.D. Mapping Local Climate Zones for a Worldwide Database of the Form and Function of Cities. *ISPRS Int. J. Geo-Inf.* **2015**, *4*, 199–219. [CrossRef]
36. Ren, C.; Cai, M.; Wang, R. Local Climate Zone (LCZ) Classification Using the World Urban Database and Access Portal Tools (WUDAPT) Method: A Case Study in Wuhan and Hangzhou. *Urban Heat Islands* **2016**, 56–67.
37. Perera, N.; Emmanuel, R. A “Local Climate Zone” based approach to urban planning in Colombo, Sri Lanka. *Urban Clim.* **2018**, *23*, 188–203. [CrossRef]
38. Gál, T.; Bechtel, B.; Lovovics, E. Comparison of two different Local Climate Zone mapping methods. *Int. Conf. Urban Clim.* **2015**, 342–351.
39. Davenport, A.; Grimmond, C.; Oke, T. The revised Davenport roughness classification for cities and sheltered country. In Proceedings of the 15th conference on probability and statistics in the atmospheric sciences/12th conference on applied climatology, Asheville, NC, USA, 8–11 May 2000; pp. 14–18.
40. Xu, E.Y.; Ren, C.; Cai, M.; Edward, N.Y.Y.; Wu, T. Classification of Local Climate Zones Using ASTER and Landsat Data for High-Density Cities. *IEEE J. Sel. Top. Appl. Earth Obs. Remote Sens.* **2017**, *10*, 1–9. [CrossRef]
41. Tsunematsu, N.; Yokoyama, H.; Honjo, T.; Ichihashi, A.; Ando, H.; Shigyo, N. Relationship between land use variations and spatiotemporal changes in amounts of thermal infrared energy emitted from urban surfaces in downtown Tokyo on hot summer days. *Urban Clim.* **2016**, *17*, 67–79. [CrossRef]
42. Perini, K.; Magliocco, A. Effects of vegetation, urban density, building height, and atmospheric conditions on local temperatures and thermal comfort. *Urban For. Urban Green.* **2014**, *13*, 495–506. [CrossRef]
43. Wang, R.; Cai, M.; Ren, C.; Bechtel, B.; Xu, Y.; Ng, E. Detecting multi-temporal land cover change and land surface temperature in Pearl River Delta by adopting local climate zone. *Urban Clim.* **2019**, *28*, 100455. [CrossRef]
44. Yang, J.; Jin, S.; Xiao, X.; Jin, C.; Xia, J.C.; Li, X.; Wang, S. Local climate zone ventilation and urban land surface temperatures: Towards a performance-based and wind-sensitive planning proposal in megacities. *Sustain. Cities Soc.* **2019**, *47*, 101487. [CrossRef]
45. Tan, P.Y.; Bin Ismail, M.R. Building shade affects light environment and urban greenery in high-density residential estates in Singapore. *Urban For. Urban Green.* **2014**, *13*, 771–784. [CrossRef]
46. Kotharkar, R.; Bagade, A. Local Climate Zone classification for Indian cities: A case study of Nagpur. *Urban Clim.* **2018**, *24*, 369–392. [CrossRef]

